



# Microstructural development during additive manufacturing of biomedical grade Ti-6Al-4V alloy by three-dimensional binder jetting: material aspects and mechanical properties

Abdolreza Simchi<sup>1,2</sup> · Frank Petzoldt<sup>2</sup> · Thomas Hartwig<sup>2</sup> · Sebastian Boris Hein<sup>2</sup> · Bastian Barthel<sup>2</sup> · Lea Reineke<sup>2</sup>

Received: 23 January 2023 / Accepted: 22 May 2023 / Published online: 30 May 2023  
© The Author(s), under exclusive licence to Springer-Verlag London Ltd., part of Springer Nature 2023

## Abstract

Additive manufacturing (AM) of biomedical materials provides enormous opportunities to fabricate multifunctional and structurally designed frameworks for tissue engineering, such as dental implants and bone substitutes. Despite several advantages of the binder jet 3D printing technology over other AM methods, for example, no limitations in materials selection, high materials recycling efficiency, no thermal stress development, no need to support materials, and the possibility of fabrication of printing functionally graded materials, the fabrication of biomedical-grade titanium alloys with high-density, fine microstructure, and low pickup of impurities is still challenging. This work presents the effects of powder particle size and 3D printing conditions on the microstructural features and mechanical properties of Ti-6Al-4V alloy. The formation of large and inter-aggregate pores during binder jetting is demonstrated and discussed. Design and selection of particle size distribution with a mean diameter of  $\sim 20 \mu\text{m}$  and large span and positive skewness are proposed to minimize binder-induced powder aggregation and fabricate green parts with a density of  $65 \pm 1\%$  PFD (pore-free density). Dilatometric studies under a partial pressure of argon (0.1 bar) determine that sintering just above the  $\alpha/\beta$  transus temperature ( $\sim 980 \text{ }^\circ\text{C}$ ) provides a high strain rate to remove pores, but high-temperature sintering ( $\geq 1250 \text{ }^\circ\text{C}$ ) is required to attain 97% PFD. The successful fabrication of high-density Ti-6Al-4V parts ( $\geq 96\%$  PFD) with the microstructure comparable to metal injection molding (MIM) titanium parts ( $\approx 100 \mu\text{m}$   $\alpha$  grains +  $\beta$  lattes) is demonstrated. The tensile strength and elongation values fall in the range of  $880 \pm 50 \text{ MPa}$  and  $6 \pm 2\%$  (depending on the processing condition), which is comparable with metal injection molded parts and superior to the laser powder bed fusion technology concerning ductility. The content of carbon ( $< 0.02 \text{ wt.}\%$ ) and nitrogen ( $0.01 \text{ wt.}\%$ ) also falls in the standard region of metal injection molding. However, oxygen pickup during sintering moderately increases the oxygen content (for 30–50%) over the standard level. The concentration of interstitials entrapped in the metal is comparable to that of parts manufactured by the powder bed fusion process, but the mechanical properties are better matched with the commercial titanium alloy. The fabrication of the titanium alloy as per the ASTM F2885 standard provides an excellent opportunity for the binder jetting process to develop custom-made biomaterials.

**Keywords** Powder-based additive manufacturing · Titanium alloy · Sintering · Binder-metal interaction · Metallic biomaterial

✉ Abdolreza Simchi  
simchi@sharif.edu

Frank Petzoldt  
frank.petzoldt@ifam.fraunhofer.de

Thomas Hartwig  
thomas.hartwig@ifam.fraunhofer.de

Sebastian Boris Hein  
sebastian.boris.hein@ifam.fraunhofer.de

Bastian Barthel  
bastian.barthel@ifam.fraunhofer.de

Lea Reineke  
lea.reineke@ifam.fraunhofer.de

<sup>1</sup> Department of Materials Science and Engineering,  
Sharif University of Technology, Azadi Avenue,  
Tehran 14588 89694, Iran

<sup>2</sup> Fraunhofer Institute for Manufacturing Engineering  
and Applied Materials Research (IFAM), Wiener Str. 12,  
28359 Bremen, Germany

## 1 Introduction

Among the seven categories of AM technologies [1], the binder jetting process offers on-demand manufacturing of complex-shaped parts without almost any limitations in materials selection and requirements to support structures. As no thermal stresses are developed during manufacturing, shape distortion and cracking by residual stresses are also prevented [2]. Besides, no intensive energy input is utilized to create undesirable or anisotropic microstructural features either by rapid cooling (typically in the order of  $10^3$  to  $10^6$  K s<sup>-1</sup> for fusion AM) depending on the type of process and fabrication conditions, for example, Ref. [3, 4], or material loss due to evaporation [5]. Moreover, the material recycling efficiency is high, which offers cost-effectiveness compared to many other AM methods, particularly for expensive materials. Furthermore, it is theoretically feasible to print any type of alloy and compounds by mixing different powders that provide an excellent opportunity for material development for niche and high-tech applications. By employing multiple print heads and incorporating nanoparticles in the binder or alternating the composition of the powder bed in different layers, quick fabrication of functionally graded materials is also possible [6]. Despite all these advantages, difficulties can arise due to the large shrinkage during de-binding and sintering which can lead to part distortion and warpage. 3D printing of green specimens with higher density and uniform pore structure can mitigate these difficulties.

During the binder jetting process, an adhesive liquid is spread on a thin powder bed layer by iterative ink-jet printing. The liquid binds the powder particles together locally, and through layer-by-layer powder deposition and ink-jet printing, complex-shaped parts embedded in the powder bed are produced. The printed bed is then cured to obtain green parts. After de-powdering, the green parts are sintered at a desired temperature for densification or infiltrated with a third material to attain a composite with high structural durability and functionality [7]. So far, this process has successfully been employed for AM of (i) metals and alloys including iron alloys, particularly 316 stainless steel [8–10], copper [11, 12], Ni-based superalloys (alloy 625 and alloy 718) [13, 14], titanium (pure Ti) [15, 16], cobalt alloys (Co-28Cr-6Mo and Co-30Cr-4.5W) [17–19], and magnetic materials and magnetic shape alloys (Fe-6Si, FeNdB, and Ni-Mn-Ga) [20–22]; (ii) ceramics, including alumina, silica, calcium phosphates, bioactive glasses, tungsten carbides, and plasters [3]. Despite the significant advantages of the binder jetting process, the processed materials are indeed a few. This shortcoming may partly be due to several parameters that affect the quality of the printed parts, including density, dimensional accuracy,

surface finish, microstructure, and mechanical properties. The characteristics of the binder system, the printing strategy, binder curing, and the sintering process affect the properties and quality of the products.

Titanium and its alloys are used in biomedical implants due to their excellent biological performance, such as biocompatibility (non-toxic and low allergenic properties) and osseointegration [23]. It is pertinent to point out that the Ti system is complex; hence, the properties of Ti alloys greatly vary with the chemical composition, level of impurities, phase constitution, grain size, etc. [24, 25]. Nevertheless, demands for orthopedic implants (artificial knees, hip joints, elbows, bone plates, and screws for fracture fixation), as well as dental implants (removable prostheses, maxillofacial prostheses, and supporting materials), are increasing. The advantageous physical, chemical, and mechanical properties of titanium alloys have also made them a unique candidate for lightweight and corrosion-resistant biomedical devices in pacemakers and artificial hearts [26]; however, other alloy systems may be used. According to ISO 5832 standards, 26 groups of titanium alloys have been used in biomedical applications; among them, Ti6Al4V (grade 5) is the most commonly used [27]. This grade is heat treatable with a decent combination of properties and fabricability. The implants are commonly produced by powder metallurgy, CAD-driven machining of cast or wrought bars, and metalworking techniques [28].

Recently, AM with titanium alloys has been executed, aiming to produce custom-made implants (e.g., hip joints). Powder bed fusion technologies, including laser powder bed fusion (PBF-LB/M), electron beam melting (EBM), selective laser sintering (SLS), and 3D laser cladding, have been examined to fabricate desired parts by fusing titanium particles at specified locations [27, 29]. Although these methods are up-and-coming, disadvantages such as expensive runs, low surface finish quality, undesirable microstructural development, low material efficiency, and process duration limit their application in large-scale production cycles [30]. Considering the advantages of binder jetting over fusion-based AM technologies, it becomes apparent that binder jet additive manufacturing of titanium alloys offers excellent opportunities for the small-scale production of custom-made biomedical devices. However, to the best of our knowledge, there are few reports in the open literature on the binder jetting of titanium and titanium alloys. Recently, İyibilgin and Gepek [31] have shown that the sintering of CP-Ti parts fabricated by binder jetting at 1200 °C in argon yields a density of ~92%. The relatively low density of the manufactured parts results in an inferior mechanical strength compared to the conventional powder metallurgy method. Basalah et al. [32, 33] have studied the effects of layer thickness (62–175 µm) and sintering temperature (800–1400 °C) on the microstructure and densification of CP-Ti. Porous

samples (17–44%) with a compressive strength ranging from 27 to 509 MPa have been fabricated as a bone substitute. Sheydaeian et al. [15] have examined binder jetting of CP-Ti at various process parameters. They have shown that particle segregation during powder deposition along with anisotropic shrinkage during sintering is challenging. Their findings have affirmed the results of Wheat et al. [34], which have employed computer tomography to visualize the effect of particle size distribution on the density and microstructure of green and sintered CP-Ti samples. Polozov et al. [35] have recently attempted to fabricate Ti-22Al-25Nb alloy by binder jetting of mixed elemental powders followed by high-temperature reactive sintering (800–1100 °C) and subsequent annealing at 1400 °C. The microstructure consisted of a B2/ $\beta$ -phase with acicular Ti<sub>2</sub>AlNb precipitates. Miyanaji et al. [36] have proposed a physics-based model to predict the optimal saturation level for binder jet printing of Ti-6Al-4V alloy. Although the model's accuracy has been approved experimentally, the fabrication of functional parts has not been further investigated or reported. Stevens et al. [37] have studied binder jetting of Ti-6Al-4V alloy and shown that the sintered density at the edges and regions with significant topological curvature is lower and higher than in the other areas, respectively. The microstructural heterogeneity is ascribed to the powder-binder interactions during printing. Dilip et al. [38] have studied the feasibility of TiAl fabrication by binder jetting of Ti-6Al-4V/Al powder mixture followed by reactive sintering. They have demonstrated the formation of TiAl with various other intermediate phases. Yadav et al. [39, 40] have studied the feasibility of fabricating Ti<sub>x</sub>Al<sub>y</sub>-based composites using indirect binder jetting methods. Porous TiC/Ti6Al4V pre-forms (12–35% pores) are prepared by binder jetting, and then vacuum infiltration of aluminum is employed to prepare dense titanium aluminide parts. Sheydaeian and E. Toyserkani [41] have fabricated periodic structures based on Ti/TiB whiskers through binder jetting of titanium-reinforced with TiB<sub>2</sub> particles (highly loaded in a resin) followed by low-temperature pressure-less sintering. They have shown that increasing the sintering temperature promotes reactions between the matrix and the reinforcing particles to grow TiB whiskers with improved stiffness.

A literature survey indicates that binder jet additive manufacturing of Ti-6Al-4V has scarcely been studied because

the fabrication of high-density parts with fine and uniform microstructure is still challenging. As the printed (green) parts have low density with a heterogeneous pore structure, high-temperature sintering causes nonuniform shrinkage, part distortion, and microstructural coarsening. The need for further research originates from the fact that the quality, characteristics, and performance of the fabricated parts vary with the powder characteristics and printing parameters. Moreover, the sintering process is the state of the art to avoid porosity gradient, part deflection, microstructural coarsening, and contamination pickup. This work aims to study binder jet additive manufacturing of Ti-6Al-4V. This alloy accounts for about 50% of all applications of titanium and its alloys in the biomedical engineering [29]. We report the effect of particle size and size distribution on the green and sintered density of the titanium alloy manufactured by the binder jetting process. Furthermore, a useful strategy to fabricate high-density parts (>97%) with a relatively uniform pore structure and dimensional accuracy is presented. Moreover, microstructural features and mechanical properties of the 3D printed parts as compared to the ASTM standard for metal injection molded titanium parts are reported. Finally, the application of the binder jetting process in the small-scale production of titanium parts is demonstrated. The process allows for high capacity for the fabrication of custom-made implants through the utilization of innovative AM technology.

## 2 Materials and methods

### 2.1 Materials

To study the role of particle size, commercial Ti-6Al-4V powders (ASTM B348) with four different particle size distributions were provided by ECKART TLS Technik GmbH and AP&C (Germany). The chemical composition of the powders was (wt.%) 90.30 Ti, 5.56 Al, 4.02 V, and 0.23 Fe, according to the supplier datasheet. The powder particles had a spherical shape with the characteristics given in Table 1. The powders were produced by the electrode induction-melting gas atomization (EIGA for TLS powders) and the advanced plasma atomization (APATM for AP&C powder) techniques. Powder blending was carried out in a

**Table 1** Characteristics of Ti-6Al-4V powders. The values of density are relative to the pore-free density (PFD)

Powder	Supplier	D <sub>10</sub> (μm)	D <sub>50</sub> (μm)	D <sub>90</sub> (μm)	Apparent density (%)	Tap density (%)
A	TLS	5.0	13.6	28.3	35.2±0.3	61.7±1.2
B	TLS	8.6	19.3	30.6	39.3±0.3	58.3±1.5
C	TLS	11.0	26.5	44.6	50.5±0.6	64.2±2.2
D	AP&C	9.8	27.2	42.3	59.4±0.3	68.5±0.5

D<sub>n</sub> describes the diameter where *n*% of the distribution has a smaller particle size

TURBULA® T2F mixer (Glen Mills, USA) for an hour. Different powder blends were prepared at various weight ratios of fine to coarse particles, i.e., the addition of 20 to 80% of Powder A or Powder B to Powder D.

## 2.2 3D printing

Binder jet 3D printing was carried out on a commercial ExOne Innovent<sup>+</sup> system (USA) using the CleanFuse binder and a 30 pl printhead. The powder materials were smoothly spread over the build platform using a roller to form a skinny powder layer. The following printing parameters were employed:

- Droplet/line spacing: X drop spacing: 50.8  $\mu\text{m}$ ; Y drop spacing: 51  $\mu\text{m}$
- Print head traverse velocity: 150 mm/s
- Print passes per X jet spacing: 5
- Droplet volume (measured not nominal values from the print head): 25,9 pL
- Averaged droplet size: 37  $\mu\text{m}$
- Computed droplet frequency: 2941 Hz
- Printing saturation: variable in the range of 40 to 80% depending on the particle size determined by trial-and-error to attend sound parts with maximum green density
- Powder bed density used to calculate the saturation: 60%
- Layer thickness: variable in the range of 30 to 90  $\mu\text{m}$  depending on the printing aim
- Bed temperature: variable in the range of 40 to 60  $^{\circ}\text{C}$

Cuboid parts (Fig. 1a) with dimensions of 10×10×10 mm<sup>3</sup> were printed layer by layer at different layer thicknesses

(30–90  $\mu\text{m}$ ), bed temperatures (40–60  $^{\circ}\text{C}$ ), and binder saturation levels (40–80%). The experimental design was reported in Electronic Supplementary Information (ESI), Table S1. Several specimens were printed and the processing conditions that yielded the highest green density were selected for further analysis. After sintering, the density and shrinkage uniformity in different directions were chosen as the criteria for optimization. The ASTM B883 standard for MIM parts was considered to manufacture tensile test specimens (Fig. 1b). The gauge length and diameter of the tensile specimens after sintering were about 20 mm and 3.4 mm, respectively. To demonstrate the ability of the process for small-scale production of Ti-6Al-4V parts, a series of titanium cups (Fig. 1c) with an outer diameter of 27 mm, an inner diameter of 22 mm, and a height of 5 mm were printed.

## 2.3 Binder curing, de-binding, and sintering

The printed parts were cured in an oven at 180  $^{\circ}\text{C}$  for 4 h. The green parts were obtained by de-powdering of the job box and removal of the loose powder bed with soft brushes. De-binding and sintering were carried out in an Elnik MIM 3002 T-50 furnace with a ball valve to control the partial pressure at the inlet of a helical vacuum pump. The process was carried out under a partial pressure of argon (0.1 bar, purity > 99.999%) in a gas-tight refractory molybdenum retort with a gas management system. For de-binding, the heating rate was 3  $^{\circ}\text{C}/\text{min}$  up to 550  $^{\circ}\text{C}$  and then held for 60 min to remove the binder. For sintering, the samples were heated at a rate of 5  $^{\circ}\text{C}/\text{min}$  to the desired temperature, which varied in the range of 1000 to 1360  $^{\circ}\text{C}$ . The sintering

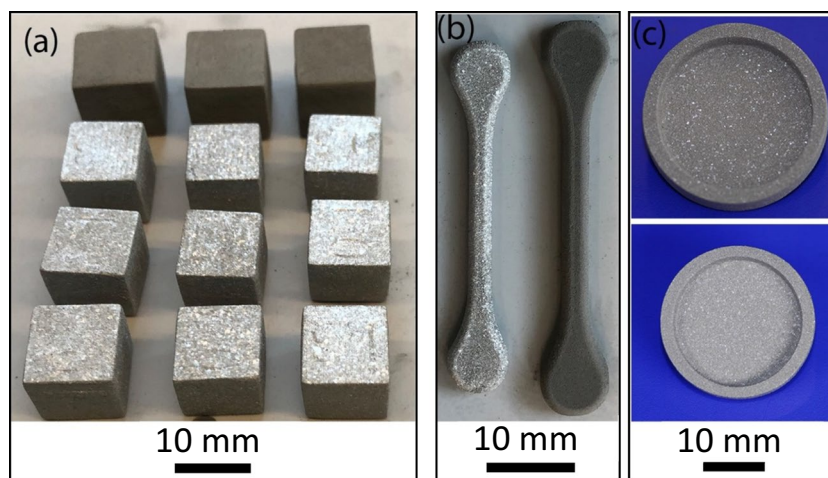


**Fig. 1** Representative optical images of titanium parts manufactured by binder jet additive manufacturing. **a** Green (top row) and sintered cubes. The dimensions of the green parts are 1×1×1 cm<sup>3</sup>. The sintered temperature was 1320  $^{\circ}\text{C}$  with a dwell time of 4 h. **b** Green (right) and sintered tensile test samples (gauge dimensions are 20 mm

and 3.4 mm). The sintering temperature was 1280  $^{\circ}\text{C}$  with a dwell time of 3 h. **c** Green (top) and sintered (down) cup-shaped specimens (outer dimension: 27 mm; inner diameter: 22 mm; height: 5 mm). The given dimensions correspond to the CAD model. The actual sizes of the samples in different images are not comparable



time was between 60 and 240 min. The cooling rate was approximately 10 °C/min.

## 2.4 Materials characterizations

A summary of characterization techniques and the samples utilized are reported in Table S2. A brief description is explained below.

### 2.4.1 Characteristics of Ti-6Al-4V powders

The size distribution of the particles was determined by a Beckman Counter Laser Particle Size Analyzer (LS 13 320 Beckman Coulter, Inc. CA, USA) in ethanol. The span of size distribution is defined as [42]:

$$\text{Span} = \frac{D_{90} - D_{10}}{D_{50}} \quad (1)$$

This parameter indicates how far  $D_{10}$  (10 pct) and  $D_{90}$  (90 pct) points are apart, normalized with  $D_{50}$  (the midpoint). The relative magnitude and direction of a distribution's deviation from the normal distribution are explained by [42]:

$$\text{Skewness} = \frac{\sum_i^N (X_i - X_m)^3}{(N - 1) \times \sigma^3} \quad (2)$$

where  $X_i$  is the volume fraction at the  $i$  percentile,  $X_m$  is the mean,  $N$  is the number of data points, and  $\sigma$  is the standard deviation.

The apparent density was measured by the Scott volumeter as per the ASTM B329 standard. The tap density (packed density) of the powders was determined by a graduated cylinder (ASTM B527 standard).

### 2.4.2 Density and sintering shrinkage

The green density (GD) was determined by the volumetric method, i.e., dividing the weight of the specimens by their volume determined by a clipper. The sintered density (SD) was measured by the water displacement method as per the ASTM B962 standard. A petroleum jelly (Vaseline®) was used to prevent the penetration of water into the surface pores. The linear and volumetric amount of the sintering shrinkage was determined by measuring the dimensions of the specimens with a vernier caliper with an accuracy of 0.01 mm.

### 2.4.3 Dilatometry

To study the sintering response of 3DBJ parts, sinter dilatometry was employed. Cuboidal parts with a cross-section of  $3 \times 3 \text{ mm}^2$  and height of 5 mm were prepared and examined

by a sinter dilatometer (DIL 402 Netzsch, Germany) under a partial pressure of argon (purity > 99.999%). The heating and cooling rates were 5 °C/min and 10 °C/min, respectively. The sintering temperature was 1350 °C with a dwell time of 240 min.

### 2.4.4 Microstructure

To visualize the pore structure of 3D printed parts, standard metallographic techniques were employed. For green parts, cubical specimens were sintered at 800 °C for 30 min. The samples were cross-sections in different directions relative to the building and printing directions. Afterward, grinding on emery papers and mechanical polishing were utilized to prepare metallographic cross-sections. The same procedure was utilized for the sintered specimens and chemical etching was carried out in an  $\text{HNO}_3/\text{HF}/\text{H}_2\text{O}$  solution. Optical and electron scanning microscopy (Leo 438 VP SEM) equipped with energy-dispersive X-ray analysis (EDX) was employed for detailed microstructural analyses.

### 2.4.5 Thermal analysis and impurity measurements

Differential scanning calorimetry (DSC) was employed to determine the phase transformation temperature of Ti-6Al-4V powders. A Linseis simultaneous thermal analyzer (TGA-DSC; Linseis Messgeraete GmbH) was utilized. A heating and cooling rate of 5 °C/min without a dwelling phase was utilized. The concentration of impurities in the sintered parts was determined by ONH 2000 and CS instruments (C/H/N/O/S elemental analysis, ELTRA).

### 2.4.6 Mechanical properties

As shown in Fig. 1b, tensile test specimens were prepared by 3D binder jetting. Uniaxial tensile testing was carried out by a Zwick instrument with a load cell of 10 kN. The applied strain rate was  $8 \times 10^{-3} \text{ s}^{-1}$ . All experiments were carried out at ambient temperature (23 °C).

### 2.4.7 Surface roughness measurements

The surface roughness of 3D printed parts as a function of the number of printed layers was evaluated. Rectangular specimens with dimensions of  $25 \times 25 \text{ mm}^2$  were printed for 2 to 6 layers. The layer thickness was 50  $\mu\text{m}$ . The surface roughness of printed parts was measured by a wide-area VR 3100 measuring system (Keyence, USA). The utilized magnification was 80 $\times$ , and a cut-off filter based on ISO 3274 and ISO 4288 was used. Five tests per sample at different places were performed. The average values of arithmetic mean height ( $S_a$ ) and maximum height ( $S_z$ ) with standard deviation were reported.

### 3 Results and discussion

#### 3.1 Effect of powder characteristics on the green density

Binder jet additive manufacturing of Ti-6Al-4V powders with different size distributions was performed to fabricate green parts with the highest possible green density. High-density green parts are favorable because they have higher strength (ease of handling) and result in denser parts after sintering with improved mechanical properties and reduced non-uniform sintering shrinkage. We have printed several parts at different processing parameters, including used powder particle sizes, the layer thickness, binder saturation, and bed temperature (as explained in Experimental Section 2.2 and Table S1), and measured the green density. The density of the printed parts varies between 56 and 64% of PFD with a standard deviation of

0.5–1.1%. For instance, the effect of mean particle size on the green density at the layer thickness of 30  $\mu\text{m}$  and bed temperature of 40  $^{\circ}\text{C}$  is shown in Fig. 2a. In agreement with other studies, for example, Ref. [7], a direct relationship between the green density and the mean particle size and powder bed density cannot be figured out because (1) powder spreading on the platform may be non-uniform and accompanied by the formation of pores due to the particle agglomeration, sticking to the roller, and jamming [43], (2) particle ejection from the powder bed induced by the impact of binder droplets [2], and (3) rearrangement of particles and formation of aggregates by the drag force of the binder (this will be explained in the following sections).

The presented results reveal that the densification of the powder bed during binder jetting is a complex process and cannot be described by a single parameter such as the mean particle size. We propose that other parameters including particle size distribution should be taken into account. As

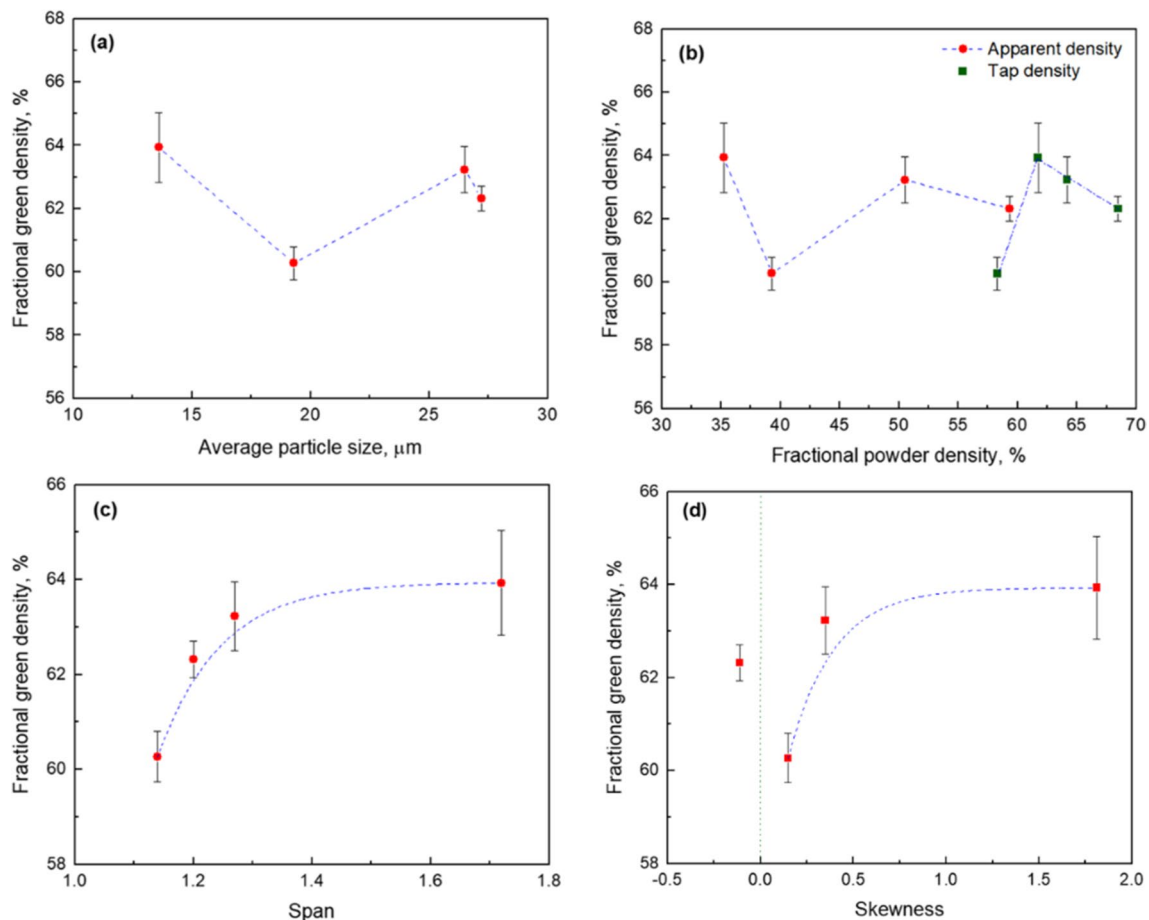


**Fig. 2** Effect of powder characteristics on the green density of 3D printed parts. **a** and **b** Effects of average particle size and powder bed density on FPD of 3D printed parts reveal no general trend for green density variation with the size and density of the powder bed. **c** A

higher green density is attained when powder particles with broader size distributions (higher span) are utilized. **d** Powders with right-hand skewness yield higher green density after 3D printing. The dash lines only show the trend of variation to aid with traceability

the powder packing depends on the size distribution profile, we have examined the effect of span (the degree of distribution width) and skewness (the degree of distortion from symmetric distribution) on the green density (Fig. 2c and d). As seen, the grain density is higher when powders with broader size distributions are utilized. Except for the coarse powder of AP&C (powder D), the size distribution of other powders exhibits a positive (right-hand) skewness and higher green density after 3D printing. We have found that the higher span and skewness are, the denser the green parts become. Despite the risk of particle segregation, a broad size distribution provides high packing density because fine particles fill the interstitial spaces between the coarse ones. With a right-hand (positive) skewness, the presence of coarse particles restricts particle movement, ejection, and aggregation during spreading and binder jetting. Therefore, we propose that a mixture of fine and coarse powders with broad size distribution is used, as described in the next section.

### 3.2 Design and selection of powder size distribution

In light of the results obtained, we propose that metal powders with a broad particle size distribution, large span, and right-hand skewness would be suitable to attain higher green density after binder jetting. For this aim, we have prepared different powder mixtures at various fine to coarse particle ratios. For instance, Fig. 3a shows the particle size distribution of the blends made of powders B ( $D_{50} \sim 19 \mu\text{m}$ ) and D ( $D_{50} \sim 27 \mu\text{m}$ ). The average particle size, skewness, and span of the blended powders as a function of the fraction of the fine powder are shown in Fig. 3b. As seen, the span reaches a maximum value of  $\sim 1.8$  for the blend containing 50% of the fine fraction. The maximum positive skewness of  $\sim 0.6$  is attained at 70% of the fine fraction. In this range of powder fraction (50–70%), the average particle size ranges between 21 and 23  $\mu\text{m}$ . The size distribution plot for the blends made of the coarse powder (D) mixed with the finer ones (A and B) are shown in Fig. 3c. Employing powder B results in a broad powder size distribution with hump distribution. In Table 2, the characteristics of powder blends with different size distributions are compared. The results indicate that the powder blend with a hump distribution has a high packing density (64% PFD), large span (1.86), and sizeable right-hand skewness (0.87). After 3D printing, the green density exceeds 65% PFD. Despite the high green density, the powder spreading is not enough to fabricate large and complex-shaped parts unless the deposition speed is reduced or the layer thickness is increased. The bimodal powder mixture yields a lower green density (about 3%), but the powder has better spreadability. These findings reveal the importance of particle size tailoring for successful 3DBJ of complex parts with a high density. The results also affirm the rational

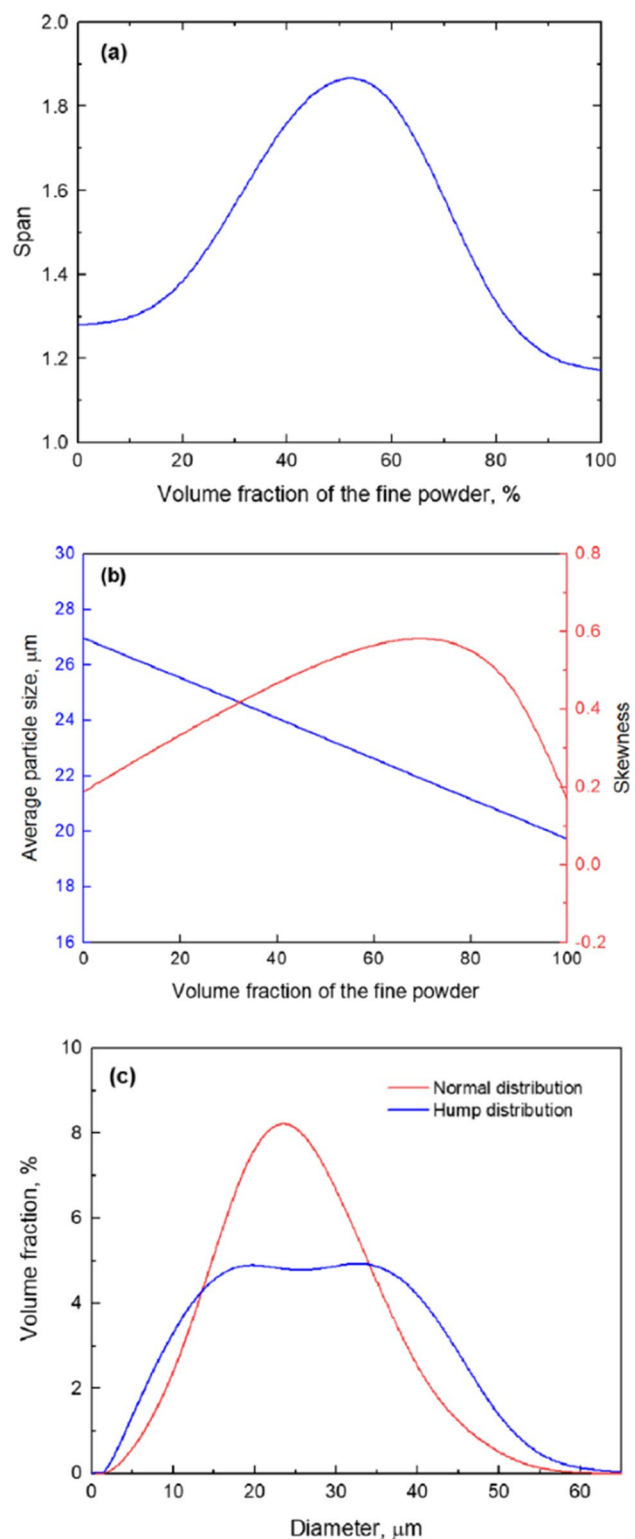


**Fig. 3** Effect of blending on the average size and size distribution of titanium alloy powders. **a** span and **b** average particle size and skewness for the powder mixer of B and D at various fractions. **c** Particle size distribution for the blends obtained from B+D (normal) and A+D powders (humps)

**Table 2** Characteristics of blended powders. The values of density are relative to PFD

Size distribution	Apparent density	Tap density	Span	Skewness	Green density
Normal	42.4±1.0	63.9±0.4	1.22	0.39	61.8±0.6
Hump	44.6±1.0	64.2±0.6	1.86	0.87	65.2±0.9

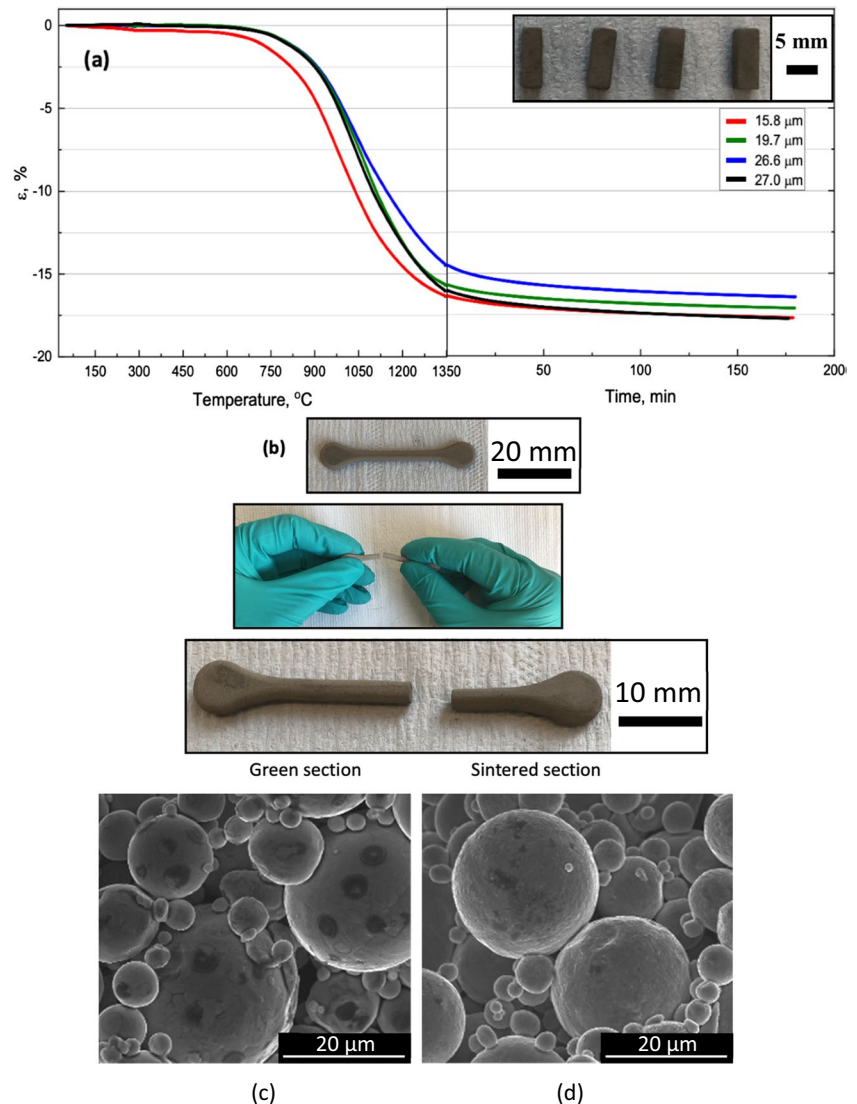
design of particle distribution, based on the span and skewness of the particles.

### 3.3 Pore structure

Besides the green density, microstructural features of printed parts concerning the size and distribution of pores are of high importance. Titanium parts with finer and uniform distribution of pores can be sintered at 1200 °C for 60 min without severe microstructural coarsening and heterogeneous shrinkage [44]. Therefore, observation of the pore structure in green parts provides valuable

information on the powder rearrangement and local densification during binder jetting. Since green parts after de-powdering and curing do not have enough strength, we employed low-temperature sintering to form sintered contacts without shrinking to keep the pore structure unchanged. Figure 4a shows the dilatometric curves of the printed parts (the inset) at 1350 °C for 4 h under the reduced pressure of argon (0.1 bar). The results determine that at around 800 °C, the amount of sintering strain ( $\epsilon$ ) is about 1%, indicating the initiation of the sintering shrinkage and formation of sintering necks [44]. Therefore, the sintered contacts should be formed without affecting the

**Fig. 4** Sintering response and microstructure of green parts. **a** Dilatometric curves of 3D printed Ti-6Al-4V parts (inset). The experiments were carried out under argon (0.1 bar) with a heating rate of 10 °C/min. **b** Images illustrate the method used to study the effect of low-temperature sintering (800 °C for 30 min) on the pore structure. SEM images show the fracture surface of **c** green and **d** sintered tensile samples. The insets show neck formation between individual particles by the binder (dark area) or sintered contacts. The pore structure is preserved after sintering. The scale bar is 20  $\mu$ m





pore structure. To confirm this hypothesis, a green tensile sample was broken from the middle of the gage length (Fig. 4b). SEM studies of the fracture surface determine a porous structure consisting of the individual powder particles (Fig. 4c).

After sintering at 800 °C for 30 min, no changes in the individual powder particles are visible but the sintered contacts are formed (Fig. 4d). Therefore, the low-sintering practice can be employed to remove the binder, form particle-particle contacts, and render enough strength for cutting the samples for metallography. Figure 5 shows representative cross-sectional metallographic images of a printed part utilizing powder D (Table 1). The sections were prepared in the X-Z direction (perpendicular to the moving print head) and Y-Z direction (perpendicular to the building direction). The images determine that the pore structure is not homogenous throughout the green part and is notably different in 2-different directions. More pores are visible in the building direction, owing to the heterogeneity of powder distribution on the printed layers and the effect of binder jetting on the deposited powder layer (e.g., movement and ejection of particles within the interaction depth) [2]. To mitigate the heterogeneous pore structure, both powder particle characteristics and binder jetting processing conditions should be tailored, as will be discussed in the following sections.

### 3.4 Large pore networks

To further study the pore formation during binder jetting, a single layer was printed on a ceramic plate, cured and the upper surface was studied by SEM (Fig. 6). The aggregation of fine particles indicates that during binder jetting, the binder droplets rearrange the particles. At the same time, its capillary force (driven by viscosity and surface tension) drags the fine portion to form aggregates with inter-aggregate pores. To study the effect of binder jetting on surface quality, roughness measurements were carried out on printed parts with different numbers of layers. Figure 7 shows the results of the measurements for powder D. The arithmetic mean height ( $S_a$ ) and maximum height ( $S_z$ ) indicate a gradually decreasing trend that levels off after a few layers. The rough and porous surface of the previous layer prevents uniform and dense deposition of the fresh layer; hence, a non-uniform pore structure is built up. Chains or networks of inter-aggregate pores are thus formed during layer-by-layer deposition. The size of the aggregates is independent of the powder particle size. However, the size of pores in inter-aggregates and intra-aggregates increases with the particle diameter. It is also pertinent to point out that the impact of binder droplets on the surface of the powder bed can also induce movement and ejection of particles within the interaction depth [2]. Therefore, three types of pores can be realized in the printed parts, including (1) intra-aggregate

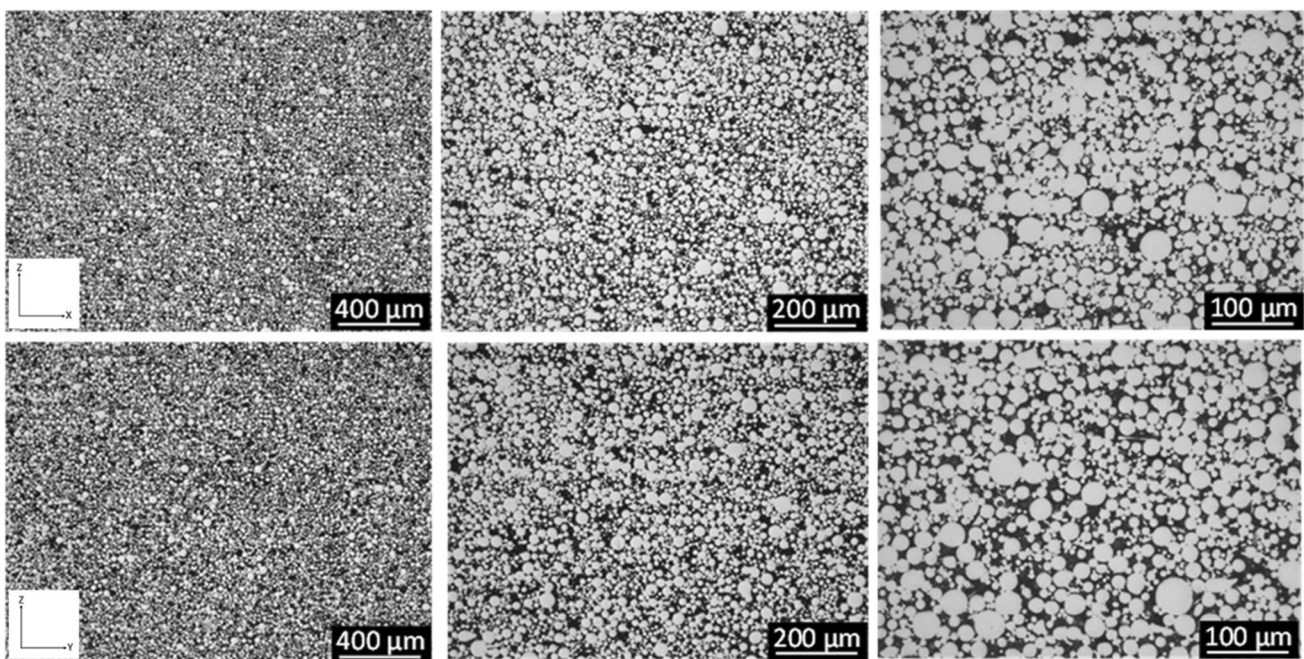
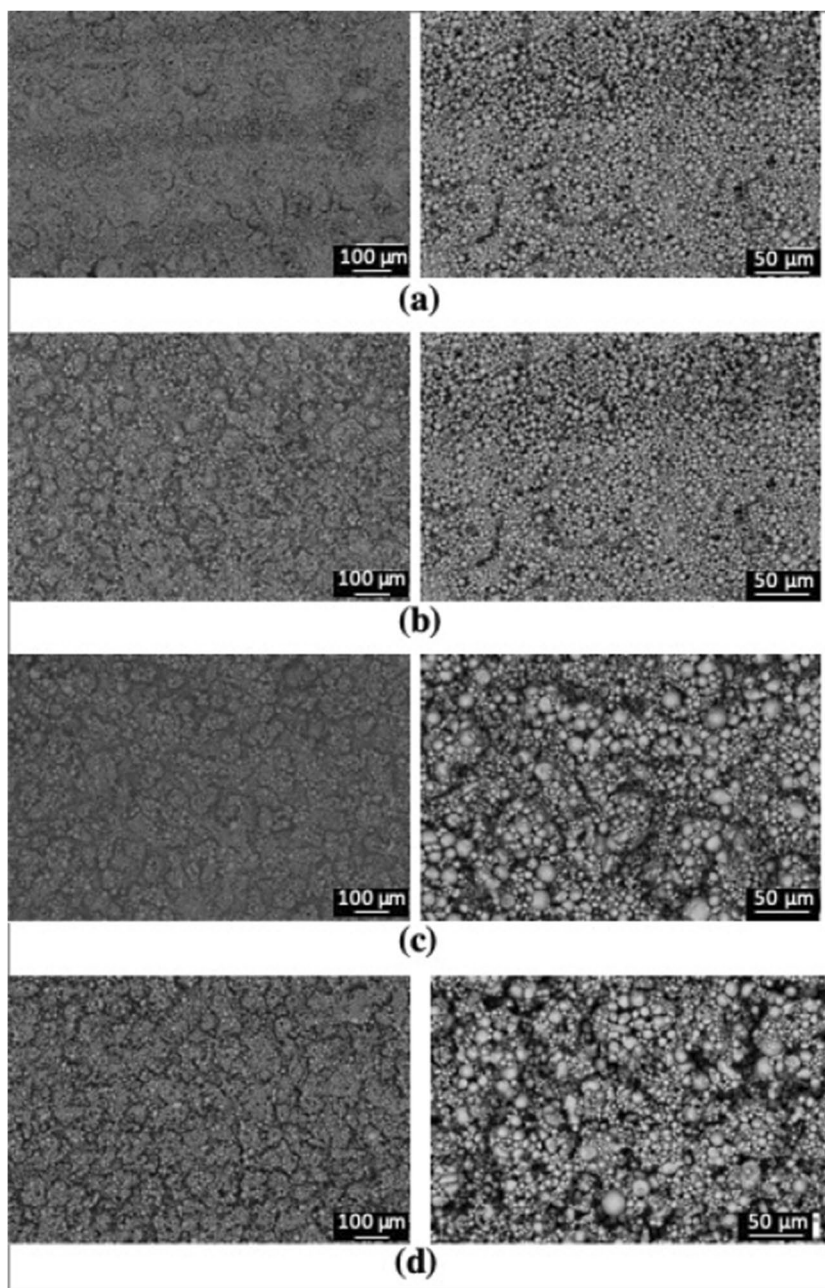


**Fig. 5** Structure of pores in green Ti-6Al-4V parts (powder D). Metallographic images show the polished cross-sections of a green part at different magnifications (the magnification increases from left to right). Low-temperature sintering (800 °C for 30 min) under an argon

atmosphere was employed to keep the pore structure unchanged. The upper and lower rows represent the cross-sections in X-Z (perpendicular to the moving printed head) and Y-Z (perpendicular to the building) directions, respectively

**Fig. 6** Binder-induced particle aggregation. SEM images show the upper surface of 3D printed parts made of powder **a** A, **b** B, **c** C, and **d** D at two different magnifications



pores that are due to the particle packing and influenced by the capillary effect of the binder, (2) inter-agglomerate pores created by the coalescence of particles and their movement by the drag force of the binder, and (3) interlayer pores that are formed during powder spreading (the particles cannot fill up the pores in the underlying layer because of size, sticking, and jamming effects). It is easier to remove the intra-aggregate pores because of their size. The inter-aggregates can form chain-like structures, and their size depends on the mean particle diameter (Fig. 6). Therefore, high-temperature sintering is required to break down the pore networks. However, interlayer pores or inter-aggregate pores that maybe

form columns of pores in the building direction are hard to be removed even during high-temperature sintering. Concerning the surface quality of the printed parts, it is pertinent to point out that the surface quality after sintering is improved but similar to other AM technologies [45], the surface quality is not ideal for multiaxial loading and must be enhanced by post-processing methods.

To affirm this hypothesis, the Ti-6Al-4V powder with the hump particle distribution (Table 2) was used to print cuboidal samples. We chose this powder because the high fine portion promotes aggregation and ejection phenomena. Sintering was carried out at different temperatures (850 °C,



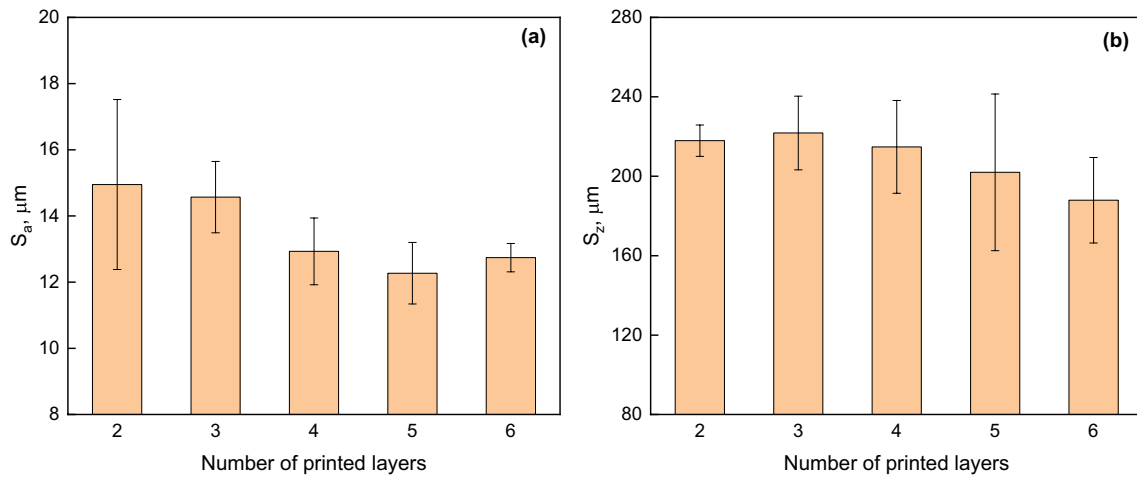
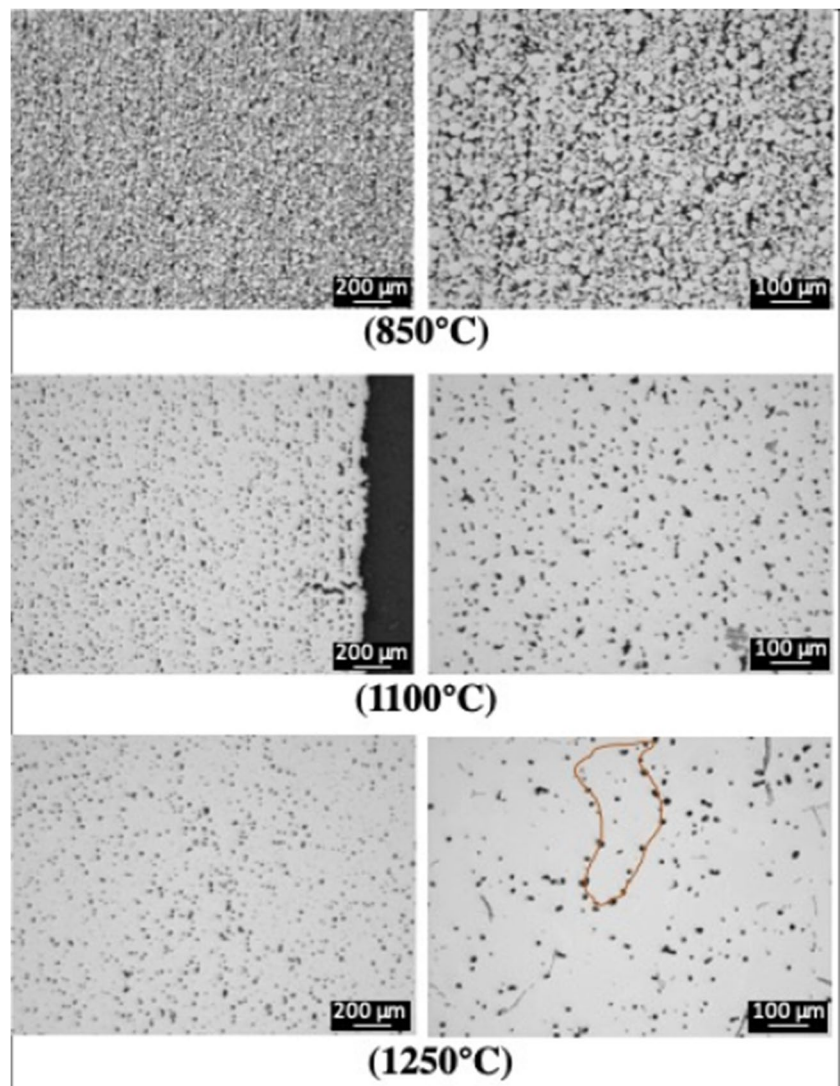


**Fig. 7** Surface roughness of 3D printed parts. **a** Variations of the arithmetic mean height and **b** maximum height for powder D depending on the number of printed layers. The vertical error bars show the standard deviation

**Fig. 8** Structure of pores in sintered Ti-6Al-4V parts. Binder jetting was carried out at a layer thickness of 30  $\mu\text{m}$  and bed temperature of 40  $^{\circ}\text{C}$ . The samples were sintered at different temperatures to track the pore closure. Microstructural images (X-Z direction) show the formation of pore chains toward the vertical direction (building direction) after binder jetting (850  $^{\circ}\text{C}$ ) that are stable up to medium temperature (1100  $^{\circ}\text{C}$ ). A high-temperature sintering practice (1250  $^{\circ}\text{C}$  for 3 h) removes most pores, but the structure of inter-aggregate pores is still detectable (marked by the red line)



1100 °C, and 1250 °C) for 3 h. Figure 8 shows representative micrographs of the pore structure. Based on the phase diagram of the Ti-6Al-4V alloy [46], the low sintering temperature below the  $\beta$ -phase region ( $<980\pm 4$  °C) preserves the pore structure of the green part because of the low sintering driving force and low sintering shrinkage (see Fig. 4a). Chains of vertically aligned pores are noticeable in line with the building direction (X-Z). Sintering at the intermediate temperature (above the  $\alpha+\beta$  transus temperature) results in pore closure but large pores mostly remain intact. Although the high-temperature sintering proceeds to high densification and breakdown of the network of inter-aggregate pores, discontinuous pores (10–20  $\mu\text{m}$ ) are visible.

To visualize the effect of binder jetting on the formation of inter-aggregate pores, cuboidal specimens with an internal bore (2 mm wide) were designed and printed (Fig. 9a). The powder that remained in the bore was not removed during de-powdering, and the composite structure (printed shell and the filled bore with particles) was sintered at a low temperature (850 °C, 30 min). Microstructural studies of the binder jetting area determine a porous structure consisting of

small and large pores (the left-hand side image of Fig. 9a). In contrast, the microstructure of the bore, which is composed of particles collected during powder spreading, is relatively dense with fewer and smaller pores (the right-hand side image of Fig. 9a). This observation affirms that the binder droplets significantly interact with the particles and induce porosity either by particle movement and ejection, formation of large aggregates by the surface tension and viscosity effect, or impairing the layer deposition. For quantification, we designed an experiment to directly measure the density of the powder bed after layer spreading. Arrays of thin-wall cups were designed and fabricated by binder jetting at different locations of the building box (Fig. 9b). The cups had a 5 mm wall thickness. Without removing the particles inside the cups during de-powdering and curing, the weight of the filled cups was measured by a balance. The cups were then fully de-powdered, and the weight difference divided by the internal volume yielded the powder bed density. Figure 9c shows the difference between the green density of the printed parts and the powder bed density at different platform locations for layer thicknesses of 40 and 90  $\mu\text{m}$ .

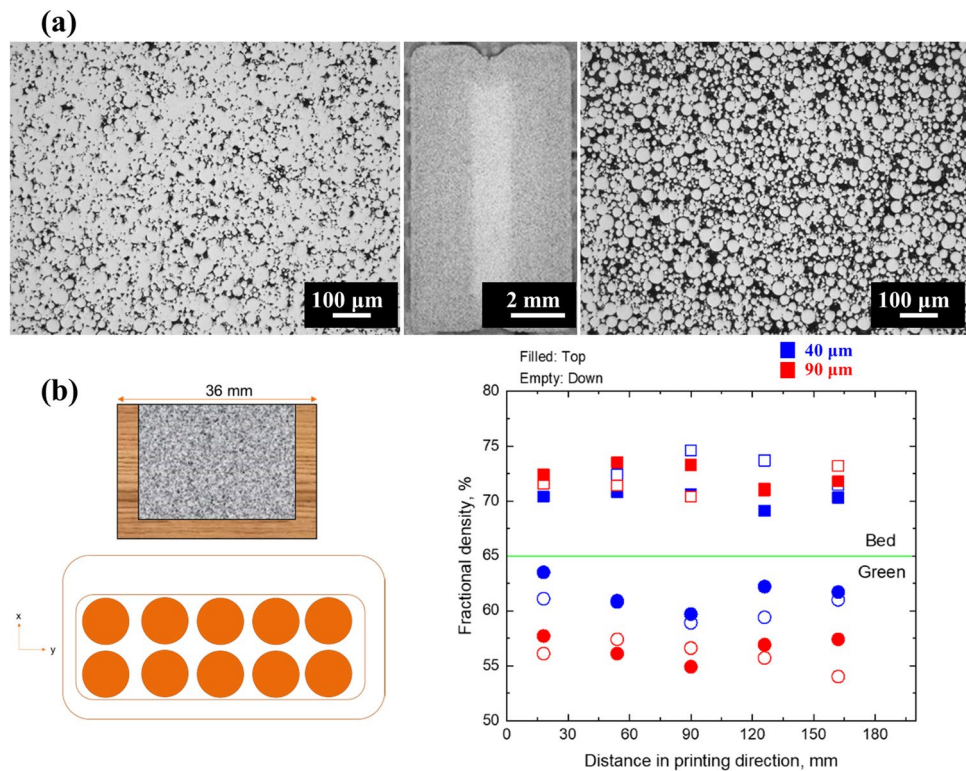


**Fig. 9** Binder-powder bed interactions form pores during 3D printing. **a** Representative microstructure of the cuboidal specimens with a small bore (2 mm) after sintering at 800 °C for 30 min (powder D). The left-hand side image shows the printed section and the right-hand side image exhibits the pore structure in the bore. **b** Schematic representation of printed cups and their arrangement on the building platform. **c** Density variations at different positions of the building platform (see image **b**). The powder was deposited at two different

layer thicknesses (40 and 90  $\mu\text{m}$ ). The upper part of the figure shows the powder bed density and the lower part of the figure displays the green density after 3D printing. The difference determines the effect of binder jetting on the formation of pores. To investigate upon the effect of position along the building directions, the samples were printed on top of each other at a distance of about 5 cm. The filled and unfilled symbols stand for the density at the top and bottom positions, respectively



Besides slight differences in the density at different positions of the platform, the difference in the local density ranges between 15 and 20%. The difference is more pronounced when a thicker layer thickness is utilized. The difference in the density at different platform locations is attributed to nonuniform powder spreading on the surface by ultrasonic shaking of the hopper (systematic instrumental error).

### 3.5 Sintering and microstructural development

The sintering response of the green (3D printed) parts was evaluated by dilatometry. The main sintering features are summarized in Table 3. The results indicate that sintering starts at around 800 °C (1% strain) and the maximum strain rate occurs at a temperature ( $T_{\text{Max}}$ ) between 990 and 1068 °C, depending on the particle size. Herein, the  $\alpha/\beta$  transition and the associated change of volume, as well as thermally-activated atom-vacancy exchanges, cause anomalous diffusion in the  $\beta$ -phase [47] that significantly enhances the strain rate. The maximum linear strain during non-isothermal sintering ranges from 14.4 to 16.4%. During isothermal sintering at 1350 °C, slight linear strain (up to 1.9%) occurs. Sintering starts at lower temperatures ( $T_s$ ) and proceeds faster for fine particles with higher sintering activity.

The densification of green parts after batch sintering at different temperatures was also studied. Figure 10a shows the apparent density of 3D printed parts (surface/open pores were not considered) after sintering at different temperatures for 3 h. It is observed that the density increases almost linearly with the inverse of mean particle size independent of the green density. Solid-state sintering is controlled by the migration of atoms via surface, grain boundaries, and volume diffusion. At the initial and medium stages of sintering, the driving force for solid-state sintering is highly influenced by the surface energy and surface curvature [48]; hence, the sintering thermodynamics is inversely proportional to the radius. At the final sintering stage, the sintering temperature has a significant influence on the densification to speed up the volume diffusion. Therefore, increasing the temperature above 1250 °C further improves the densification. The densification becomes marginal above 1300 °C because the total solid/vapor surface energy at the final stage is reduced, while

**Table 3** Sintering parameters for 3D printed Ti-6Al-4V parts. Non-isothermal sintering was carried out at a rate of 10 °C/min. Isothermal sintering at 1350 °C was carried out for 4 h

Powder	$T_s$ , °C	$T_{\text{max}}$ , °C	$\epsilon$ at $T_{\text{max}}$ , %	$\epsilon_{\text{non-isothermal}}$ , %	$\epsilon_{\text{isothermal}}$ , %
A	789	1068	10.1	16.4	1.3
B	802	1095	9.4	15.7	1.4
C	803	990	4.8	14.4	1.9
D	796	1036	7.5	16.0	1.7

grains overgrow [48]. Therefore, the sintering of Ti alloys at temperatures above 1300 °C is not favorable because of grain growth and impurity pickup.

The effect of sintering temperature on the densification of green parts prepared from coarse (D) and fine (A) powders and their mixture (bimodal powder with normal size distribution) is shown in Fig. 10b. The higher density at the low temperature (1000 °C) for the bimodal powder is attributed to the higher green density. The fine powder exhibits faster densification at elevated temperatures ( $\geq 1200$  °C) due to higher sintering activity. The final density of the mixed powder is the same as the fine powder at  $\geq 1280$  °C. This finding is important because powder spreading for fine powder particles is more complicated than the mixed powder with an average size of 20  $\mu\text{m}$ .

We also studied the volume of pores (open or closed) that remained after sintering the bimodal powder at 1300 °C for 3 h. The type of pores is not only crucial for the mechanical property assessment but also determines the applicability of hot isostatic pressing (HIP) to reach isotropic microstructure for the fabrication of high-performance titanium alloys [49, 50]. A layer thickness of 30  $\mu\text{m}$  was used, and the samples were printed at the bed temperature of 40 and 60 °C. The difference in the green density of the printed parts was  $\pm 1\%$ . Figure 10c determines that 1.5–2% of the pores are closed, and the large/inter-aggregate pores (about 3%) cannot be removed even after high-temperature sintering. Employing a higher layer thickness increases the total porosity with a gradual increase in the closed pores up to around 3% (Fig. 10d). The percentage of open pores remains almost constant above 50  $\mu\text{m}$  layer thickness. A representative microstructure of the sintered parts ( $\sim 96\%$  PFD) is shown in Fig. 11a. The pores are closed and have near-circular shapes. The size of most pores is less than 20  $\mu\text{m}$ . The matrix has a lamellar structure with a distinct region of  $\alpha$  and  $\beta$  phases. The  $\alpha$  colony size is about 100  $\mu\text{m}$ . These characteristics are almost the same as the MIM Ti-6Al-4V alloy reported in the literature, for example, Ref. [51].

### 3.6 Mechanical properties and interstitial impurities

The effect of mean particle size on the tensile strength and elongation of sintered parts is shown in Fig. 11b–d. The tensile strength varies between 830 and 930 MPa. The change in the tensile strength partly arises from differences in porosity, and the sintering temperature (1250 and 1300 °C) shows a minor influence on the results. The highest strength is attained for the powder with a mean particle size of  $\sim 20$   $\mu\text{m}$  (powder B). The ductility of the sintered parts exhibits a pronounced relationship with the sintering temperature and mean particle size. The effect of sintering temperature can be ascribed to the pore shapes, i.e., round pores are formed at higher temperatures

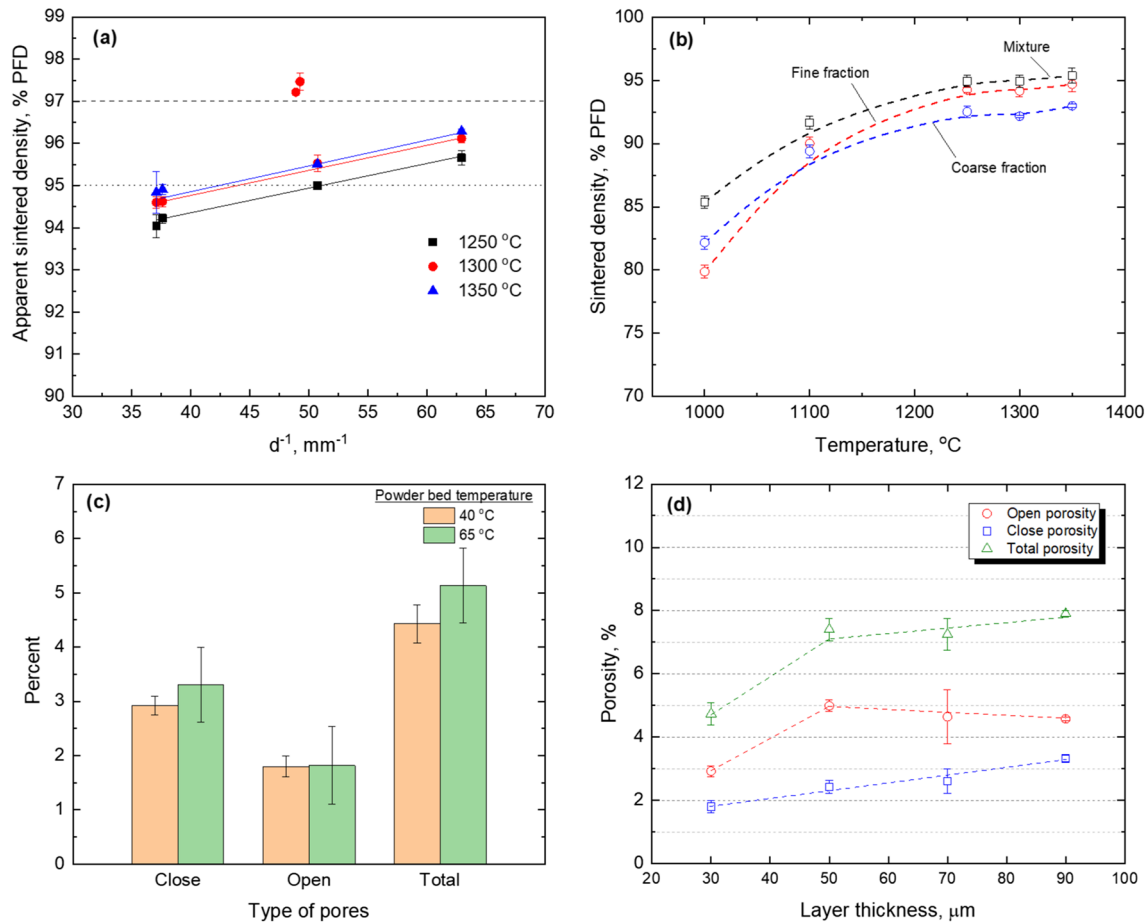


**Fig. 10** Sintering of 3D printed Ti-6Al-4V alloy. **a** Apparent sintered density as an inverse function of the mean particle size. The individual solid red dots show the density of powders with bimodal and hump size distribution sintered at 1300 °C. The green parts were fabricated at the layer thickness of 30  $\mu\text{m}$ , binder saturation of 65%, and bed temperature of 40 °C. **b** Effect of sintering temperature on the

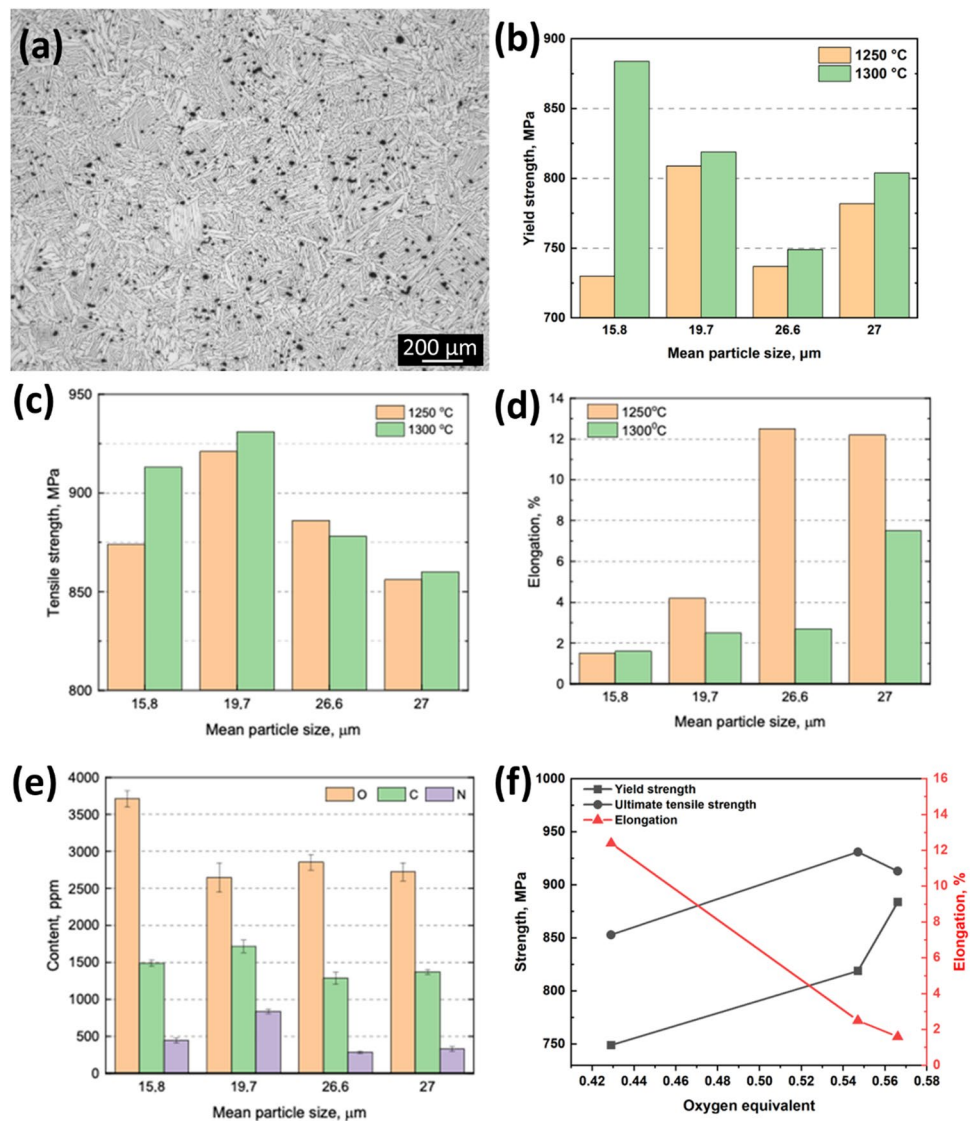
density for the coarse powder (D), fine powder (A), and their mixture (60:40 coarse to fine). The layer thickness was 50  $\mu\text{m}$ . The binder saturation was 50%. **c** The type of pores in the sintered sample for the bimodal powder mixture. **d** Effect of layer thickness on the porosity in the sintering samples. In all experiments, the sintering time was 3 h

with a less undesirable effect on the ductility [44]. The lower tensile elongation of finer particles can be attributed to the higher interstitial content (C, O, and N) (Fig. 11d). Compared with the as-received powders (C<800 ppm, N<300 ppm), the results indicate that 600–800 ppm carbon should be picked up during processing. The amount of nitrogen pickup is about 100 to 200 ppm. Carbon and nitrogen contamination vary slightly with the mean particle size and should be retrieved from the binder. However, the amount of oxygen in the sintered part is significantly higher than the as-received powders (about 1600 ppm). The high oxygen concentration indicates that the sintering atmosphere has not been pure enough for the sintering of titanium, although titanium foams have been used as a getter for protection. We proposed that the high specific surface areas of titanium foams react with oxygen to protect the specimens. Titanium and oxygen have a high chemical attraction (activity), providing substantial oxygen solubility in both the

hexagonal closed-packed (~12 wt.%) and body-centered cubic phases [52]. Upon sintering, oxygen penetrates through the surface scale into the titanium (>550 °C) and readily absorbs atmospheric oxygen above 700 °C [53]. Therefore, for the additive manufacturing of titanium, environmental control at different processing stages (powder handling, storage, 3D printing, de-binding, and sintering) is a critical requirement. Here, it is essential to mention that the amount of oxygen content in the specimens prepared by binder jetting is comparable with those made by LPBF (about 3000 ppm) [54]. Kazantseva et al. [55] have shown that on the surface of LPBF parts, the amount of oxygen and nitrogen can reach 3 wt.% and 0.05 wt.%, respectively. Based on the oxygen equivalent (OE) determined by [56]:

$$OE = \%O + 2\%N + \frac{2}{3}\%C \quad (3)$$

**Fig. 11** Microstructure, mechanical properties, and interstitial impurities in sintered Ti-6Al-4V alloy sintered at 1250 °C and 1300 °C for 3 h. **a** Representative microstructure showing distinct regions of  $\alpha$  and  $\beta$  phases with fine and uniform pore structure. Effect of particle size on the **b** yield strength, **c** tensile strength, and **d** elongation. Up to five samples were examined for tensile testing. The standard deviation of the measurements for tensile strength and elongation was less than 15 MPa and 2%, respectively. **e** The content of interstitial impurities in the sintered parts (1300 °C/3 h) under argon (0.1 bar, 99.999% purity). **f** Effect of OCE on the strength and elongation



The results indicate that OE decreases from 0.56 to 0.46% using coarser particles. The interstitials entrapped in the metal are responsible for increased tensile strength (Fig. 11e). In contrast to annealed specimens after LPBF with a tensile strength of  $1210 \pm 50$  MPa and tensile elongation of 3.9% [54], the mechanical properties of parts manufactured by binder jetting are closer to the commercial titanium alloy. Herein, it is important that the mechanical properties of the Ti alloy processed by other AM technologies highly depend on the processing conditions and post-treatment (annealing, aging, stress relieved, HIPed, machined, etc.) and fall in the range of 760–1245 MPa (ultimate tensile strength, UTS) and up to 19.5% (elongation, EL) [45]; hence, it is difficult to make a direct comparison. Nevertheless, it can be concluded that in as-built conditions, the mechanical properties of the Ti alloy prepared by 3D binder jetting are mostly in the same range (850–950 MPa UTS and 2–6% EL). It is also pertinent to point

out that the fracture mechanism of two-phase Ti6Al4V alloy under uniaxial loading is linked with plastic strain localization between the  $\alpha$  and  $\beta$  phases that results in the nucleation and growth of micro-voids [57]. Brittle fracture features with pseudo-embrittlement behavior were also reported for LPBFed Ti6Al4V alloy [58]. However, in sinter-based AM of titanium alloys, parts are not complexly dense (<97%); hence, the existing pores also contribute to the formation and propagation of microcracks. Therefore, the fracture mechanism is apparently brittle (cleavage features) with local ductile damage (dimple features).

### 3.7 Binder jet additive manufacturing of the titanium alloy

In light of the results, we designed a powder mixture and optimized the binder jetting processing parameters to

fabricate high-density parts. We selected the normal powder mixture (Table 2) for 3D printing because it had better flowability at the expense of lower green density (compared with the hump powder mixture). A series of cuboidal parts at different processing parameters were fabricated (Table S1). Suitable processing conditions were chosen based on the highest green density. Generally, it was found at a layer thickness higher than 40  $\mu\text{m}$ , the green density progressively decreased. A high binder saturation caused more impact of the binder jetting on pore formation due to the binder-particle interactions while a low binder saturation was not suitable for green strength. A high bed temperature could impair the powder deposition process. Based on a try-and-error approach, we chose a layer thickness of 40  $\mu\text{m}$ , binder saturation of 50%, and bed temperature of 40  $^{\circ}\text{C}$  to print the green parts. The transverse printhead speed was set at 150 mm/s, and the binder volume was about 30 pL. Under these conditions, green parts with  $62\pm 1\%$  PFD were attained. After binder curing at 180  $^{\circ}\text{C}$  for 4 h, de-binding was carried out at 350  $^{\circ}\text{C}$  for 30 min with a heating rate of 2  $^{\circ}\text{C}/\text{min}$ . The sintering cycle includes heating with a rate of 5  $^{\circ}\text{C}/\text{min}$  to 1280  $^{\circ}\text{C}$  and holding for 3 h, followed by cooling at a rate of 5  $^{\circ}\text{C}/\text{min}$ . The sintering atmosphere was argon (99.999%). The properties of the manufactured parts are summarized in Table 4. For comparison, the properties of Ti-6Al-4V MIM parts (ASTM F2885-11 standard) are presented. The results determine the potential of binder jet additive manufacturing of Ti-6Al-4V alloy for custom-made biomedical implants and devices. Although there is extensive literature available on the bio-performance of powder metallurgy processed Ti6Al4V which is analogous to the materials reported here, for example, Ref. [59], it is required to evaluate in vitro and in vivo responses of the manufactured parts to ensure the biocompatibility and osteogenesis response. This is the continuation of this work that will be presented in near future.

**Table 4** Properties of Ti-6Al-4V alloy prepared by binder jet additive manufacturing as compared with ASTM standard sintered parts. Three samples were tested

Property	3D binder jetting	ASTM F2885-11 standard
Density, %PFD	96.0 $\pm$ 0.4	98
Linear shrinkage, %	14.2 $\pm$ 0.2	12 to 15
Yield strength, MPa	869 $\pm$ 22	>830
Tensile strength, MPa	957 $\pm$ 15	>900
Elongation, %	6 $\pm$ 2	>10
C, ppm	1465 $\pm$ 187	<800
O, ppm	2742 $\pm$ 105	<2000
N, ppm	352 $\pm$ 81	<500

## 4 Conclusions

Binder jet additive manufacturing of biomedical grade Ti-6Al-4V alloy was studied. The role of particle size on the microstructural development, sintering response, mechanical properties, and the concentration of entrapped interstitials in the metal was shown. It was found that particle ejection from the bed surface during binder jetting and particle aggregation due to the drag force of the binder reduced the green density by 10–15%, depending on the processing condition. Microstructural studies determined that large particle aggregates with intra-aggregate and inter-aggregate pores were formed. Powders with broad size distribution (wide span) and right-hand side skewness were found to be more suitable for achieving higher green density. For instance, 3D printing of a titanium powder blend with a span of 1.22 and skewness of 0.39 yielded a high green density ( $62\pm 1\%$  PFD) with minimum inter-aggregate pores. After sintering, the inter-aggregate pores (tiny interstitial pores between particles) were readily closed during solid-state sintering above the  $\alpha/\beta$  transition temperature ( $980\pm 4$   $^{\circ}\text{C}$ ), but the inter-aggregate pores upheld stable even above 1300  $^{\circ}\text{C}$ . It was found out that sintering at 1250–1300  $^{\circ}\text{C}$  yielded parts with a density of  $\sim 96\pm 1\%$  PFD with a microstructure similar to MIM Ti ( $\alpha/\beta$  with an average grain size of about 100  $\mu\text{m}$ ). Meanwhile, moderate carbon (600–800 ppm) and nitrogen (100–200 ppm) pickup were observed. Uniaxial tensile testing indicated properties comparable with the ASTM F2885 standard. The higher tensile strength ( $957\pm 15$  MPa) and lower ductility ( $6\pm 2\%$ ) were mainly attributed to the higher oxygen equivalent (OE, 0.46–0.55%).

**Supplementary Information** The online version contains supplementary material available at <https://doi.org/10.1007/s00170-023-11661-1>.

**Authors' contributions** Abdolreza Simchi: conceptualization, methodology, investigation, formal analysis, data curing, validation, writing—original draft, and writing—review and editing. Frank Petzoldt: conceptualization, resources, project administration, and financial acquisition. Thomas Hartwig: formal analysis and data curation. Sebastian Boris Hein: visualization, data curation, and writing—review and editing. Bastian Barthel: visualization and software.

**Funding** AS acknowledges the Alexander von Humboldt Foundation for granting a research fellowship to carry out this study at the Fraunhofer IFAM institute. He also thanks Sharif University of Technology for providing facilities to perform complementary analyses (QA970816). The authors certify that they have no affiliations with or involvement in any organization or entity with any financial or non-financial interest in the subject matter or materials discussed in this manuscript.

## Declarations

**Conflict of interest** The authors declare no competing interests.



## References

- Gibson I, Rosen D, Stucker B (2015) Additive manufacturing technologies: 3D printing, rapid prototyping, and direct digital manufacturing, second edition. Johnson Matthey Technol Rev 59:193–198. <https://doi.org/10.1007/978-1-4939-2113-3>
- Parab ND, Barnes JE, Zhao C et al (2019) Real time observation of binder jetting printing process using high-speed X-ray imaging. Sci Rep 9:2499. <https://doi.org/10.1038/s41598-019-38862-7>
- Zuo X, Zhang W, Chen Y et al (2022) Wire-based directed energy deposition of NiTiTa shape memory alloys: microstructure, phase transformation, electrochemistry, X-ray visibility and mechanical properties. Addit Manuf 59:103115. <https://doi.org/10.1016/j.addma.2022.103115>
- Li B, Wang L, Wang B et al (2022) Electron beam freeform fabrication of NiTi shape memory alloys: crystallography, martensitic transformation, and functional response. Mater Sci Eng A 843:143135. <https://doi.org/10.1016/j.msea.2022.143135>
- Mostafaei A, Elliott AM, Barnes JE et al (2021) Binder jet 3D printing—process parameters, materials, properties, modeling, and challenges. Prog Mater Sci 119:100707. <https://doi.org/10.1016/j.pmatsci.2020.100707>
- Moon J, Caballero AC, Hozer L et al (2001) Fabrication of functionally graded reaction infiltrated SiC-Si composite by three-dimensional printing (3DP™) process. Mater Sci Eng A 298:110–119. [https://doi.org/10.1016/s0921-5093\(00\)01282-x](https://doi.org/10.1016/s0921-5093(00)01282-x)
- Barthel B, Hein SD, Aumund-Kopp C, Petzoldt F (2019) Influence of particle size distribution in metal binder jetting – Effects on the properties of green and sintered parts. In: Euro PM2019 Congress & Exhibition. Maastricht, Netherlands
- Rishmawi I, Salarian M, Vlasea M (2018) Tailoring green and sintered density of pure iron parts using binder jetting additive manufacturing. Addit Manuf 24:508–520. <https://doi.org/10.1016/j.addma.2018.10.015>
- Ziaee M, Tridas EM, Crane NB (2017) Binder-jet printing of fine stainless steel powder with varied final density. JOM 69:592–596. <https://doi.org/10.1007/s11837-016-2177-6>
- Verlee B, Dormal T, Lecomte-Beckers J (2012) Density and porosity control of sintered 316L stainless steel parts produced by additive manufacturing. Powder Metall 55:260–267. <https://doi.org/10.1179/0032589912Z.00000000082>
- Kumar A, Bai Y, Eklund A, Williams CB (2017) Effects of hot isostatic pressing on copper parts fabricated via binder jetting. Procedia Manufacturing, pp 935–944
- Bai Y, Wagner G, Williams CB (2017) Effect of particle size distribution on powder packing and sintering in binder jetting additive manufacturing of metals. J Manuf Sci Eng Trans ASME 139:1–15. <https://doi.org/10.1115/1.4036640>
- Nandwana P, Elliott AM, Siddel D et al (2017) Powder bed binder jet 3D printing of Inconel 718: densification, microstructural evolution and challenges. Curr Opin Solid State Mater Sci 21:207–218. <https://doi.org/10.1016/j.cossms.2016.12.002>
- Mostafaei A, Behnamian Y, Krimer YL et al (2016) Effect of solutionizing and aging on the microstructure and mechanical properties of powder bed binder jet printed nickel-based superalloy 625. Mater Des 111:482–491. <https://doi.org/10.1016/j.matdes.2016.08.083>
- Sheydaei E, Fishman Z, Vlasea M, Toyserkani E (2017) On the effect of throughout layer thickness variation on properties of additively manufactured cellular titanium structures. Addit Manuf 18:40–47. <https://doi.org/10.1016/j.addma.2017.08.017>
- Wiria FE, Shyan JYM, Lim PN et al (2010) Printing of titanium implant prototype. Mater Des 31:S101–S105. <https://doi.org/10.1016/j.matdes.2009.12.050>
- Dourandish M, Simchi A, Godlinski D (2008) Rapid manufacturing of Co-Cr-Mo implants by three-dimensional printing process for orthopedic applications. Iran J Pharm Sci 4:31–36
- Dourandish M, Godlinski D, Simchi A (2007) 3D printing of bio-compatible PM-materials. Mater Sci Forum 534–536:453–456. <https://doi.org/10.4028/www.scientific.net/msf.534-536.453>
- Mostafaei A, Rodriguez De Vecchis P, Buckenmeyer MJ et al (2019) Microstructural evolution and resulting properties of differently sintered and heat-treated binder-jet 3D-printed Stellite 6. Mater Sci Eng C 102:276–288. <https://doi.org/10.1016/j.msec.2019.04.011>
- Paranthaman MP, Shafer CS, Elliott AM et al (2016) Binder jetting: a novel NdFeB bonded magnet fabrication process. JOM 68:1978–1982. <https://doi.org/10.1007/s11837-016-1883-4>
- Caputo MP, Berkowitz AE, Armstrong A et al (2018) 4D printing of net shape parts made from Ni-Mn-Ga magnetic shape-memory alloys. Addit Manuf 21:579–588. <https://doi.org/10.1016/j.addma.2018.03.028>
- Cramer CL, Nandwana P, Yan J et al (2019) Binder jet additive manufacturing method to fabricate near net shape crack-free highly dense Fe-6.5 wt.% Si soft magnets. Heliyon 5:e02804. <https://doi.org/10.1016/j.heliyon.2019.e02804>
- Khorasani AM, Goldberg M, Doeven EH, Littlefair G (2015) Titanium in biomedical applications—properties and fabrication: a review. J Biomater Tissue Eng 5:593–619. <https://doi.org/10.1166/jbt.2015.1361>
- Salvador CAF, Maia EL, Costa FH et al (2022) A compilation of experimental data on the mechanical properties and microstructural features of Ti-alloys. Sci Data 9:188. <https://doi.org/10.1038/s41597-022-01283-9>
- Callegari B, Oliveira JP, Aristizabal K et al (2020) In-situ synchrotron radiation study of the aging response of Ti-6Al-4V alloy with different starting microstructures. Mater Charact 165:110400. <https://doi.org/10.1016/j.matchar.2020.110400>
- Olin C (2001) Titanium in cardiac and cardiovascular applications. In: Titanium in medicine: Material Science, Surface Science, Engineering, Biological Responses and Medical Applications. Springer-Verlag, Berlin Heidelberg GmbH, Berlin, pp 889–908
- Tamayo JA, Riascos M, Vargas CA, Baena LM (2021) Additive manufacturing of Ti6Al4V alloy via electron beam melting for the development of implants for the biomedical industry. Heliyon 7:e06892. <https://doi.org/10.1016/j.heliyon.2021.e06892>
- Zhang LC, Chen LY (2019) A review on biomedical titanium alloys: recent progress and prospect. Adv Eng Mater 21:1801215. <https://doi.org/10.1002/adem.201801215>
- Qian M, Xu W, Brandt M, Tang HP (2016) Additive manufacturing and postprocessing of Ti-6Al-4V for superior mechanical properties. MRS Bull 41:775–783. <https://doi.org/10.1557/mrs.2016.215>
- Nichols MR (2020) The pros & cons of powder bed fusion. Met Powder Rep 76:1–2. <https://doi.org/10.1016/j.mprp.2020.04.004>
- Osman İ, Gepek E (2021) Characterization of CP-titanium produced via binder jetting and conventional powder metallurgy. Rev Metal 57:e205. <https://doi.org/10.3989/revmetal.205>
- Basalah A, Esmaeili S, Toyserkani E (2016) On the influence of sintering protocols and layer thickness on the physical and mechanical properties of additive manufactured titanium porous bio-structures. J Mater Process Technol 238:341–351. <https://doi.org/10.1016/j.jmatprotec.2016.07.037>
- Basalah A, Shanjani Y, Esmaeili S, Toyserkani E (2012) Characterizations of additive manufactured porous titanium implants. J Biomed Mater Res - Part B Appl Biomater 100(B):1970–1979. <https://doi.org/10.1002/jbm.b.32764>
- Wheat E, Vlasea M, Hinebaugh J, Metcalfe C (2018) Data related to the sinter structure analysis of titanium structures fabricated

- via binder jetting additive manufacturing. *Data Br* 20:1029–1038. <https://doi.org/10.1016/j.dib.2018.08.135>
35. Polozov I, Sufiiarov V, Shamshurin A (2019) Synthesis of titanium orthorhombic alloy using binder jetting additive manufacturing. *Mater Lett* 243:88–91. <https://doi.org/10.1016/j.matlet.2019.02.027>
  36. Miyajima H, Zhang S, Yang L (2018) A new physics-based model for equilibrium saturation determination in binder jetting additive manufacturing process. *Int J Mach Tools Manuf* 124:1–11. <https://doi.org/10.1016/j.ijmactools.2017.09.001>
  37. Stevens E, Schloder S, Bono E et al (2018) Density variation in binder jetting 3D-printed and sintered Ti-6Al-4V. *Addit Manuf* 22:746–752. <https://doi.org/10.1016/j.addma.2018.06.017>
  38. Dilip JJS, Miyajima H, Lassell A et al (2017) A novel method to fabricate TiAl intermetallic alloy 3D parts using additive manufacturing. *Def Technol* 13:72–76. <https://doi.org/10.1016/j.dt.2016.08.001>
  39. Yadav P, Bock T, Fu Z et al (2019) Novel hybrid printing of porous TiC/Ti6Al4V composites. *Adv Eng Mater* 21:1900336. <https://doi.org/10.1002/adem.201900336>
  40. Yadav P, Fu Z, Knorr M, Travitzy N (2020) Binder jetting 3D printing of titanium aluminides based materials: a feasibility study. *Adv Eng Mater* 22:2000408. <https://doi.org/10.1002/adem.202000408>
  41. Sheydaei E, Toyserkani E (2018) Additive manufacturing functionally graded titanium structures with selective closed cell layout and controlled morphology. *Int J Adv Manuf Technol* 96:3459–3469. <https://doi.org/10.1007/s00170-018-1815-2>
  42. Merkus HG (2009) Particle size measurements: fundamentals, practice, quality. Springer Science+Business Media B.V
  43. Chen H, Wei Q, Zhang Y et al (2019) Powder-spreading mechanisms in powder-bed-based additive manufacturing: experiments and computational modeling. *Acta Mater* 179:158–171. <https://doi.org/10.1016/j.actamat.2019.08.030>
  44. Nor NHM, Muhamad N, Ihsan AKAM, Jamaludin KR (2013) Sintering parameter optimization of Ti-6Al-4V metal injection molding for highest strength using palm stearin binder. In: *Proceedia Engineering*. Elsevier B V, pp 359–364
  45. Liu S, Shin YC (2019) Additive manufacturing of Ti6Al4V alloy: a review. *Mater Des* 164:107552. <https://doi.org/10.1016/j.matdes.2018.107552>
  46. Composition C, Properties P (2020) ATI 6-4: Ti-6Al-4V alloy. *Alloy Dig* 69:Ti-171. <https://doi.org/10.31399/asm.ad.ti.171>
  47. Nakajima H, Koiwa M (1991) Diffusion in titanium. *ISIJ Int* 31:757–766. <https://doi.org/10.2355/isijinternational.31.757>
  48. German RM (1996) Sintering: theory and practice, 1st edn. Wiley-Interscience
  49. Benzing J, Hrabe N, Quinn T et al (2019) Hot isostatic pressing (HIP) to achieve isotropic microstructure and retain as-built strength in an additive manufacturing titanium alloy (Ti-6Al-4V). *Mater Lett* 257:126690. <https://doi.org/10.1016/j.matlet.2019.126690>
  50. Bolzoni L, Ruiz-Navas EM, Zhang D, Gordo E (2012) Modification of sintered titanium alloys by hot isostatic pressing. *Key Eng Mater* 520:63–69. <https://doi.org/10.4028/www.scientific.net/KEM.520.63>
  51. German RM (2013) Progress in titanium metal powder injection molding. *Materials (Basel)* 6:3641–3662. <https://doi.org/10.3390/ma6083641>
  52. Murray JL, Wriedt HA (1987) The O-Ti (oxygen-titanium) system. *J Phase Equilibria* 8:148–165. <https://doi.org/10.1007/BF02873201>
  53. Bignolas JB, Bujor M, Bardolle J (1981) A study of the early stages of the kinetics of titanium oxidation by auger electron spectroscopy and mirror electron microscopy. *Surf Sci* 108:L453–L459. [https://doi.org/10.1016/0039-6028\(81\)90442-8](https://doi.org/10.1016/0039-6028(81)90442-8)
  54. Nikiel P, Wróbel M, Szczepanik S et al (2021) Microstructure and mechanical properties of titanium grade 23 produced by selective laser melting. *Arch Civ Mech Eng* 21:152. <https://doi.org/10.1007/s43452-021-00304-5>
  55. Merkushev A, Ilyinikh M, State F et al (2017) Effect of oxygen and nitrogen contents on the structure of the ti-6al-4v alloy manufactured by selective laser melting. In: *Proceedings III International Scientific Conference: Material Science. Nonequilibrium Phase Transformations*, pp 101–103
  56. Ogden HR, Jaffee RI (1955) The effects of carbon, oxygen and nitrogen on the mechanical properties of titanium and titanium alloys. *Titan Metall Lab* 20:101
  57. Zhang XC, Zhong F, Shao JB et al (2016) Failure mechanism and mode of Ti-6Al-4V alloy under uniaxial tensile loading: experiments and micromechanical modeling. *Mater Sci Eng A* 676:536–545. <https://doi.org/10.1016/j.msea.2016.09.019>
  58. Moridi A, Demir AG, Caprio L et al (2019) Deformation and failure mechanisms of Ti-6Al-4V as built by selective laser melting. *Mater Sci Eng A* 768:138456. <https://doi.org/10.1016/j.msea.2019.138456>
  59. do Prado RF, Esteves GC, ELDS S et al (2018) In vitro and in vivo biological performance of porous Ti alloys prepared by powder metallurgy. *PLoS One* 13:e0196169. <https://doi.org/10.1371/journal.pone.0196169>

**Publisher's note** Springer Nature remains neutral with regard to jurisdictional claims in published maps and institutional affiliations.

Springer Nature or its licensor (e.g. a society or other partner) holds exclusive rights to this article under a publishing agreement with the author(s) or other rightsholder(s); author self-archiving of the accepted manuscript version of this article is solely governed by the terms of such publishing agreement and applicable law.